

DOCTORAL THESIS

Thesis Title

Author:

Ana ANDRES-ARROYO

Supervisor:

Dr. First LAST

A thesis submitted in fulfilment of the requirements for the degree of
Doctor of Philosophy



School of Physics, Faculty of Science

August 2018

Dedicated to someone.

“Fancy Quote”

Author

Abstract

School of Physics, Faculty of Science, UNSW Australia

Doctor of Philosophy

Thesis Title

by Ana ANDRES-ARROYO

Write your abstract here .

Acknowledgements

The acknowledgements and the people to thank go here, don't forget to include your project advisor...

Contents

Dedicatory	iii
Quotation	v
Abstract	vii
Acknowledgements	viii
Contents	ix
List of Figures	xi
Abbreviations	xiii
Physical Constants	xv
Symbols	xvii
1 Introduction	1
1.1 Section title	2
1.2 Compiling instructions	2
1.3 References	2
2 Using Fourier transform phase for the measurement of radial velocity	3
2.1 Phase analysis of Fourier transform for the measurement of line shift . . .	5
2.1.1 Translation property of Fourier transform	5
2.1.2 Intuitive explanation	6
2.1.3 Practical Use	7
Concluding remarks	7
2.1.4 Initial tests	7
Impact of noise	9
Concluding remarks	10
2.2 Using the Fourier transform to probe line deformation	11
2.2.1 Theory	11
2.2.2 SOAP Simulations	12
Remark	14
Remark	15
2.2.3 Jitter model	16

2.2.4	Testing the recovery of Jitter	17
2.2.5	End-to-end Simulations	18
2.3	Fourier transform with real observations	22
2.3.1	HD189733: Rossiter–McLaughlin effect as jitter	22
	Remarks	24
2.3.2	Examples 2	24
2.3.3	Example 3	24
2.4	References	24

List of Figures

1	Introduction	1
2	Using Fourier transform phase for the measurement of radial velocity	3
2.1	Translation property of Fourier transform	6
2.2	100 shifted HARPS-like line profiles	8
2.3	Fourier transform of 100 shifted line profiles	9
2.4	Radial velocity recovery	10
2.5	Fourier transform of a line profile in a complex plane	11
2.6	Deformed line profile	12
2.7	Fourier transform of deformed line profile	13
2.8	Apparent RV of deformed line profile	13
2.9	Low-pass and high-pass filters	14
2.10	Fourier transform in response to line deformation	15
2.11	Scaling the low-pass and high-pass Fourier transformed radial velocities .	16
2.12	Jitter model	19
2.13	Corner plots of MCMC	20
2.14	Planet recovery	21
2.15	Distribution of recovered parameters	21
2.16	Demo: Rossiter–McLaughlin effect	22
2.17	HD189733: removal of Rossiter–McLaughlin effect as jitter	23

Abbreviations

2D Two-Dimensional

3D Three-Dimensional

Physical Constants

Speed of Light c = $2.997\,924\,58 \times 10^8 \text{ ms}^{-\text{s}}$ (exact)

Constant Name Symbol = Constant Value (with units)

Symbols

f	focal length	mm or cm
H	heating	K/W
I	intensity	a.u.
k	trap stiffness	pN/ μ m/mW
n	refractive index	—
P	power	mW
T	temperature	$^{\circ}$ C or K
ε	permittivity	???
κ	trap stiffness	pN/ μ m/mW
λ	wavelength	nm
μ	permeability	???
σ	cross section	???
θ	tilt angle	degrees or radians

¹Chapter 1

Introduction

1.1	Section title	2
1.2	Compiling instructions	2
1.3	References	2

1.1 Section title

Always put labelthesection after each section so the page headers work. [?]

This is a test.

1.2 Compiling instructions

1. make the main file the masted document: options -i make current file masted document
2. Quick build from anywhere (because it quick builds from the master document
3. BibTex from the chapter file (disable the master document option for this and do it from "normal mode")
4. Quick build 3 times (from the master document): 1 for the text, 2 for the references and labels, 3 for the bibliography backreferencing.

1.3 References

¹ Chapter 2

Using Fourier transform phase for the measurement of radial velocity

2.1	Phase analysis of Fourier transform for the measurement of line shift	5
2.1.1	Translation property of Fourier transform	5
2.1.2	Intuitive explanation	6
2.1.3	Practical Use	7
	Concluding remarks	7
2.1.4	Initial tests	7
	Impact of noise	9
	Concluding remarks	10
2.2	Using the Fourier transform to probe line deformation	11
2.2.1	Theory	11
2.2.2	SOAP Simulations	12
	Remark	14
	Remark	15
2.2.3	Jitter model	16
2.2.4	Testing the recovery of Jitter	17
2.2.5	End-to-end Simulations	18
2.3	Fourier transform with real observations	22
2.3.1	HD189733: Rossiter–McLaughlin effect as jitter	22
	Remarks	24

2.3.2	Examples 2	24
2.3.3	Example 3	24
2.4	References	24

CGT: This needs a bit more helpful an introduction. That is WHY the fourier transform is being explored as a way to measure radial velocity. and specifically, so that you can try to tell the difference between bulk line shifts, and line profile deformations. I think the folloing does a slightly better job of that.

This chapter introduces a new method for measuring radial velocities. Specifically, it uses the Fourier transform of a line profile (or cross-correlation profile) to try and distinguish between the effects of a bulk shift in that profile (i.e. a radial velocity shift of the profile), opposed to a change in the line profile shape which can produce an apparent radial velocity shift. We examine the impact on the Fourier transformed components of a line profile of both bulk line shifts, and line profile deformations, with the aim of developing tools to distinguish between these two cases.

2.1 Phase analysis of Fourier transform for the measurement of line shift

2.1.1 Translation property of Fourier transform

The translation of a function (in our case a spectral line profile) can be examined in both its original real space, and in its Fourier transformed space. Because Fourier techniques are often used to handle time domain data, this shift in real space can be variously considered described as either time shifting or translation. In this chapter we will use “time shifting”, “translation” and “velocity shifting” interchangeably to refer to a shift of a function in real space. We will refer to Fourier transformed functions as being in the “frequency domain” regardless of whether they have actual dimensions of 1/time, 1/length or 1/velocity.

Let us consider a function $h(x)$ be a signal $f(x)$ delayed (or shifted) by an amount x_0 :

$$h(x) = f(x - x_0). \quad (2.1)$$

In the frequency domain, we will then have

$$\hat{h}(\xi) = e^{-2\pi i x_0 \xi} \hat{f}(\xi), \quad (2.2)$$

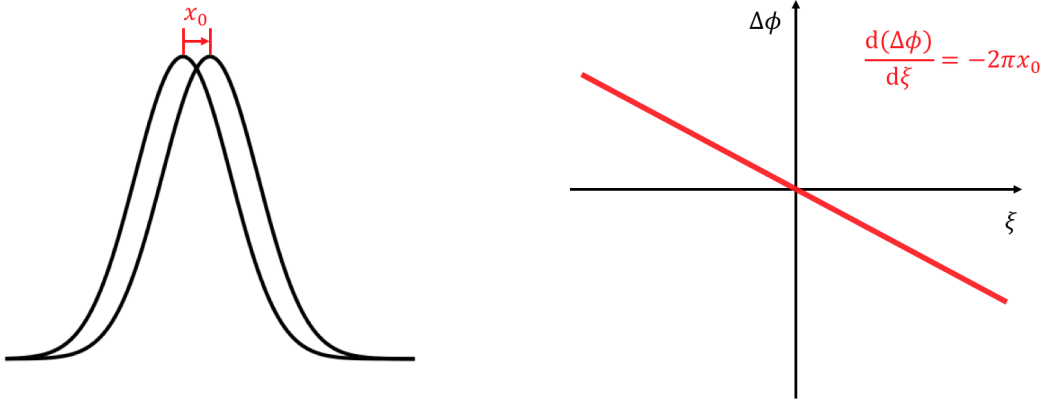


Fig. 2.1: The left panel shows a signal (or a spectral line profile in the following context) shifted by an amount x_0 . The right panel is the differential phase spectral density diagram (i.e. differential phase spectrum). The model shows a perfectly linear correlation between $\Delta\phi(\xi)$ and ξ with the constant slope $-2\pi x_0$.

where the circumflex denotes the Fourier transform of a function. $\hat{h}(\xi)$ and $\hat{f}(\xi)$ will therefore differ by a frequency dependent phase angle:

$$\Delta\phi(\xi) = -2\pi x_0 \xi, \quad (2.3)$$

while the power spectral density will remain unchanged (as $|e^{-2\pi i x_0 \xi}|^2 = 1$).

2.1.2 Intuitive explanation

The translation property of the Fourier transform follows mathematically from the nature of the transform. A (perhaps) more intuitive way to see this is that since the Fourier transform is defined

$$\hat{f}(\xi) = \int_{-\infty}^{\infty} f(x) e^{-2\pi i x \xi} dx, \quad (2.4)$$

it decomposes the function $f(x)$ into a frequency representation $\hat{f}(\xi)$, such that the function $f(x)$ is expressed as the sum of *all* the orthogonal basis $e^{2\pi i x \xi}$ times a set of their components $\hat{f}(\xi)$ (i.e. by the inverse Fourier transform):

$$f(x) = \int_{-\infty}^{\infty} \hat{f}(\xi) e^{2\pi i x \xi} d\xi. \quad (2.5)$$

This means that shifting $f(x)$ by x_0 is equivalent to shifting *all* the orthogonal basis functions by x_0 , which becomes $e^{2\pi i (x-x_0)\xi} = e^{2\pi i x \xi} \cdot e^{-2\pi i x_0 \xi}$. This is how the

$e^{-2\pi i x_0 \xi}$ term in Eq. 2.2 arises – it quantifies this phase difference.¹

The fact that the power spectrum density remains the same can also intuitively be seen, because shifting the signal as a whole doesn’t add or remove any frequency information.

2.1.3 Practical Use

From Eq. 2.3, we see that the phase shift $\Delta\phi(\xi)$ is proportional to the frequency ξ with a constant gradient or slope²

$$\frac{d(\Delta\phi)}{d\xi} = -2\pi x_0 \quad (2.6)$$

Obtaining this (in principle) is straightforward via a simple linear regression model fit to a plot of $\Delta\phi(\xi)$ versus ξ (see e.g. Fig. 2.1), so that

$$x_0 = -\frac{1}{2\pi} \frac{d(\Delta\phi)}{d\xi} \quad (2.7)$$

By analogy with the definition of power spectral density, we describe $\phi(\xi)$ the “phase spectral density” and hence $\Delta\phi(\xi)$ the “differential phase spectral density”.

Concluding remarks In principle then, an analysis of the phase shift in the frequency domain of the Fourier components of a line profile will provide a means of measuring a bulk line shift in real space.

2.1.4 Initial tests

We performed an initial test to determine whether we can correctly recover known shifts of a line profile from an analysis of the phase shift in the frequency domain of the Fourier transform of shifted line profiles.

We generated a spectral line profile based on the cross-correlation function of observed HARPS spectra with the software SOAP 2.0 *CGT: Referece*. This was replicated

¹For a simplified vision bridging a shift of the signal in the time domain and a phase difference in the frequency domain, imagine any real continuous function is a sum of sines and cosines. Changing the phase angle in the sines and cosines results in shifts in the function.

²We use Δ to refer to the phase difference between a shifted line profile and an unshifted / referenced line profile, while the derivative to refer to the response of $\Delta\phi$ to ξ .

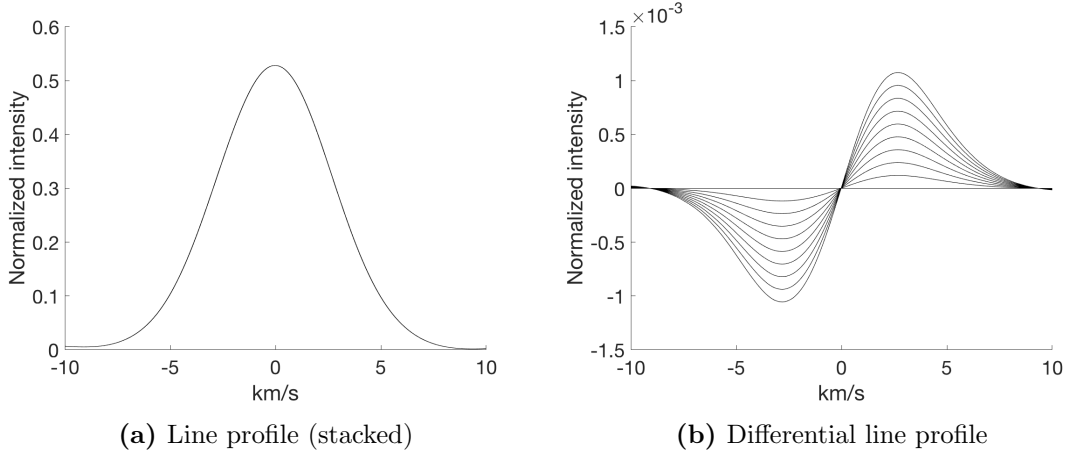


Fig. 2.2: (a) the shifted line profiles plotted on top of each other, showing that the ± 0 -10 m/s shifts are very small compared to the line profile width. (b) the shifted line profiles with the unshifted line profile subtracted from each. Note that for demonstration clarity, noise is not included in this differential line profile plot and only 10 out of 100 profiles are presented.

100 times, with a very small amount of noise (equivalent to a $S/N = 10,000$ in the line profiles) injected. These profiles were then subjected to radial velocity shifts evenly spaced between 0 and 10 m/s (Fig. 2.2).

The Fourier transform of these 100 spectral line profiles divides the information into two parts: (1) the power spectra (Fig. 2.3a) and (2) the phase spectra (shown in Fig. 2.3b as the differential phase spectra relative to the phase spectrum for the unshifted line profile).

*CGT: whereas the frequency ranges plotted in 2.2a and 2.2b are the same [are they really? are you sure the axis on 2.2b should not be in m/s instead of km/s?] , the ranges plotted in 2.3a and 2.3b are different. You don't really say why. Until later when you make comments about "noise". I suggest you should make both the plots over the same range, and then *point out* the impact of noise, and why you have chosen to limit your fits to a smaller frequency range (and justify that choice),*

We see that most Fourier transform information is concentrated in the lower frequency range in the power spectrum. The differential phase spectra are expected linear (as Fig. 2.1 demonstrated). Its deviation from linearity comes from the noise that we injected, which will be discussed later.

The slope of each differential phase spectrum indicates the shift of each line profile relative to the unshifted line profile. It should be weighted by the amplitude of the power,

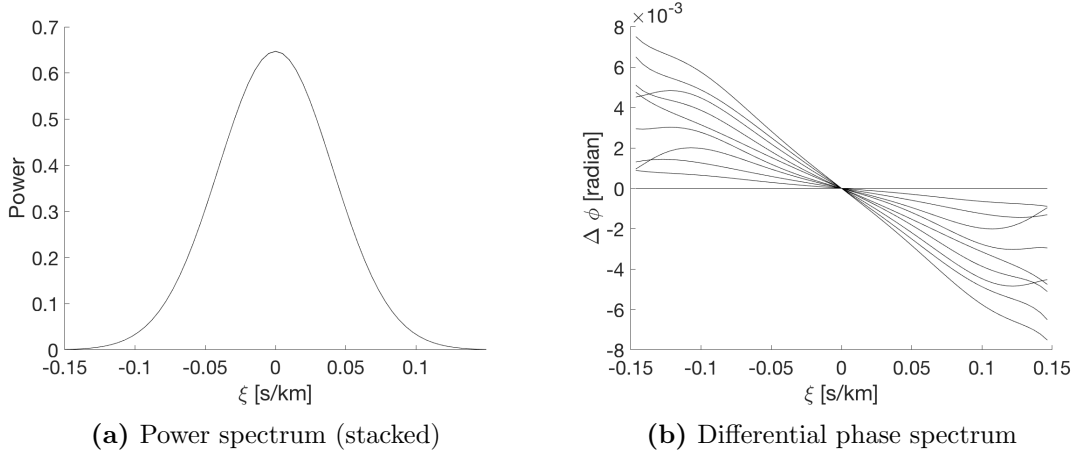


Fig. 2.3: The Fourier transform of these shifted line profile divides the information in each into (a) their power spectra and (b) their phase spectra (here plotted differential compared to that of the unshifted profile). A line shift in the time domain produces an unchanged power spectrum in the frequency domain. It does, however, produce phase shift which we see as linear trends in the differential phase spectra as a function of frequency. Note that for demonstration clarity, only 10 out of 100 differential phase spectra are presented.

meaning the lower frequencies are higher weighted. We therefore calculate the radial velocity shift for each shifted line profile using two methods:

1. the RV_{FT} using Eq. 2.7, weighted by the power spectrum
2. the RV_{Gaussian} as traditionally measured from the line centroid by fitting a Gaussian to each line profile.

We can then compare the results with the (known) input line shift where we see the expected strong 1:1 correlation (Fig. 2.4). The root-mean-square (rms) of the residuals are both $rms_{\text{FT}} = rms_{\text{Gaussian}} = 0.08$ m/s, identical up to two decimal places, indicating the expected radial velocities are consistently reduced. In addition, the fact that the two methods are so coherently different from the input radial velocity (by a small amount), as shown in the residual of Fig. 2.4, means that such deviation comes from the photon noise intrinsic to the line profile rather than the methods themselves.

CGT: How do these compare with what you'd expect from the S/N and the intrinsic line width (should say at some point what the intrinsic line width is).

Impact of noise We briefly mentioned above that the deviation from linearity in the differential phase spectrum arises from the photon noise injected in the simulated

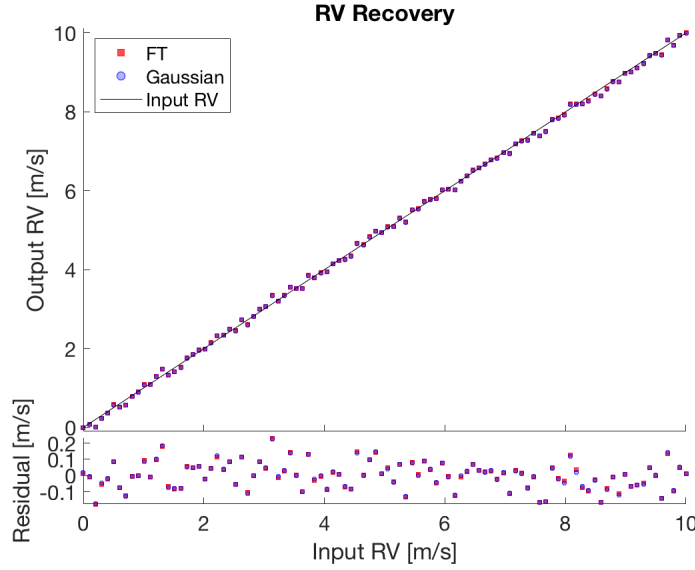


Fig. 2.4: Radial velocity recovery of line shifts with both methods: Fourier transform and Gaussian fit. Both results are highly consistent with each other.

line profile. This can be explained with the Fourier transformed line profile $\hat{h}(\xi)$ in a complex plane (also known as the Argand plane; Fig. 2.5). What we see is $\hat{h}(\xi)$ literally plotted on the complex plane – of each complex number $\hat{h}(\xi)$, the argument returns the phase angle and the square of the absolute value returns the power, for that particular frequency ξ . For larger powers ($\hat{h}(\xi)$ far from the origin), the presence of noise hardly alters the phase angle; for lower powers ($\hat{h}(\xi)$ distributed in the vicinity of the origin), a slight displacement of $\hat{h}(\xi)$ in the complex plane means a considerable change in the phase angle. It justifies using the Fourier transform spectral power to be the weight of each frequency, and introducing a cut-off frequency when making a linear fit of the differential phase spectrum.

Concluding remarks These initial tests confirm our expectation – it is possible to measure a radial velocity from the Fourier phase spectrum, and this provides an alternative to the traditional means of obtaining the radial velocities via centroiding the line profile in real space. In a broader context, this method will be applicable to measuring shifts of any pattern, and can be extended to higher dimensions. In this thesis, we primarily focus on its use to measure radial velocity shifts in spectral line profiles, and especially whether the Fourier transform phase velocity is more robust against the influence of changes in line deformation than traditional techniques.

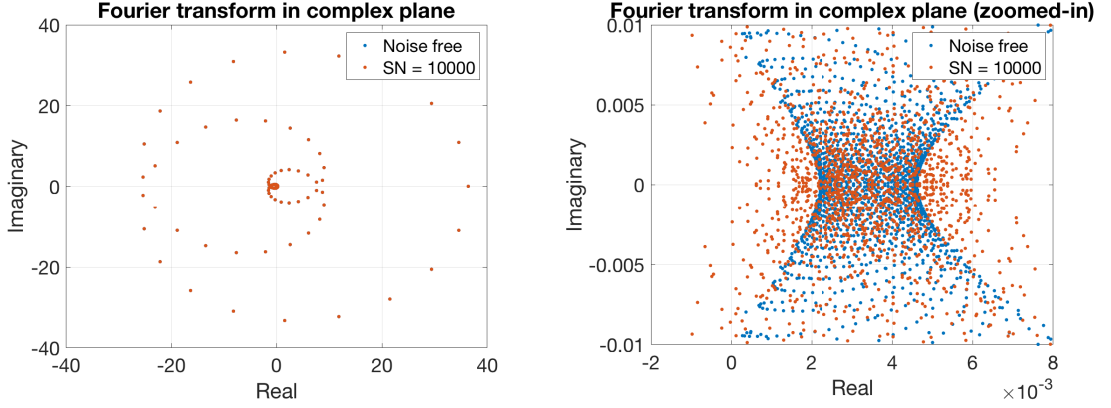


Fig. 2.5: The Fourier transform of a line profile in a complex plane.

2.2 Using the Fourier transform to probe line deformation

2.2.1 Theory

We wish to test whether this new method for measuring radial velocities is more robust against spurious apparent radial velocity shifts produced by changes in the line profile shape in an emitting stars, rather than actual line profile shifts due to a bulk motion of the emitting star. In § 2.1, the same shift x_0 applies to *all* the basis functions. In the case of line deformation due to stellar variability, x_0 becomes frequency dependent ³. That is to say, basis functions at different frequencies would shift by different amounts, resulting in shape changes (e.g. skewness) in the line profile. Therefore we modify the translation property of Fourier transform by rewriting x_0 as $x_0(\xi)$ in Eq. 2.3:

$$\Delta\phi(\xi) = -2\pi x_0(\xi)\xi. \quad (2.8)$$

As a result, the local gradient of the differential phase spectrum becomes

$$\frac{d(\Delta\phi)}{d\xi} = -2\pi\left(x_0 + \frac{dx_0}{d\xi}\right), \quad (2.9)$$

which reduces to Eq. 2.6 when x_0 is a constant as in the case of a bulk line shift. Note that the dependency of ξ has been taken out of $\Delta\phi(\xi)$ and $x_0(\xi)$ in writing the differential equation above.

³excluding the case where the result of a line deformation is exactly the same as a line shift, as this becomes indistinguishable by any means

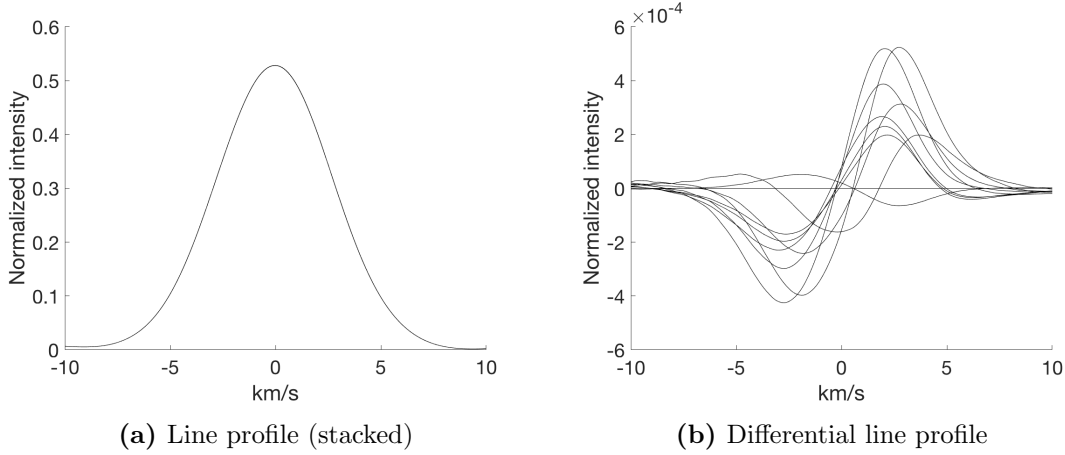


Fig. 2.6: Deformed line profile. For the sake of clarity, noise is not included in the differential line profile plot and only 10 out of 100 profiles are presented.

In principle, we could numerically solve this differential equation based on the measured local gradient $d(\Delta\phi)/d\xi$ to obtain $x_0(\xi)$. As a simplistic approach, if $x_0(\xi)$ changes with ξ slowly within a certain frequency range, we can make the approximations that $x_0 \sim \text{const}$ and $dx_0/d\xi \sim 0$. With this, Eq. 2.9 converges back to Eq. 2.6.

2.2.2 SOAP Simulations

With SOAP 2.0, we injected three spots with different longitudes, latitudes and sizes (Table 2.1) to model an emitting star, and generate 100 cross-correlation functions for the resulting deformed line profiles evenly sampled throughout the rotation period of the star (Fig. 2.6). A very small amount of noise (equivalent to a $S/N = 10,000$) was also added into the line profiles. We then take the same approach as in § 2.1 to obtain the power spectrum and (differential) phase spectrum (Fig. 2.7) to recover the radial velocities RV_{FT} . It notes, line deformation contributes to a skewed differential phase spectrum, as predicted in §2.2.1.

	Longitude	Latitude	Size in disk area percentage
Spot 1	174°	-14°	0.18%
Spot 2	288°	74°	0.40%
Spot 3	51°	52°	0.50%

Table 2.1: Spot configurations

In this case, the input radial velocities would be the apparent radial velocities of deformed line profiles (also known as jitter). Both velocities RV_{FT} and RV_{Gaussian}

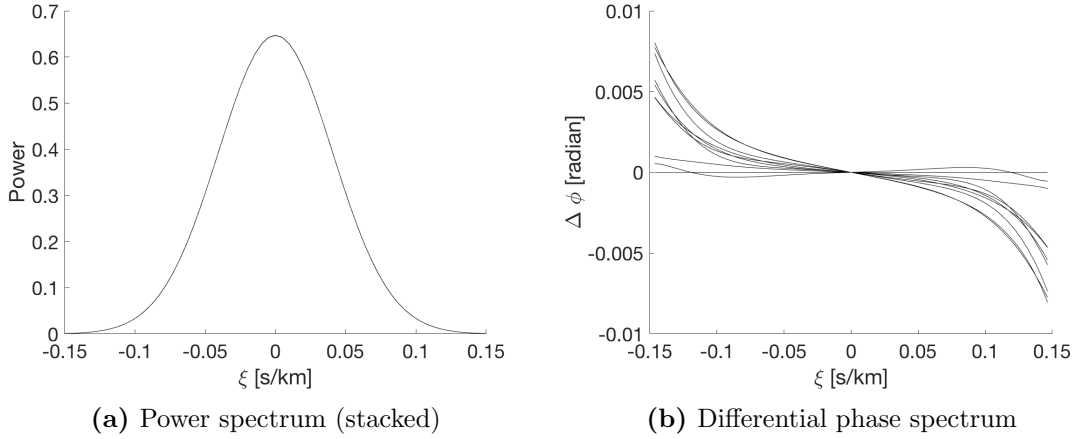


Fig. 2.7: Fourier transform of deformed line profile. Only 10 out of 100 differential phase spectra are presented.

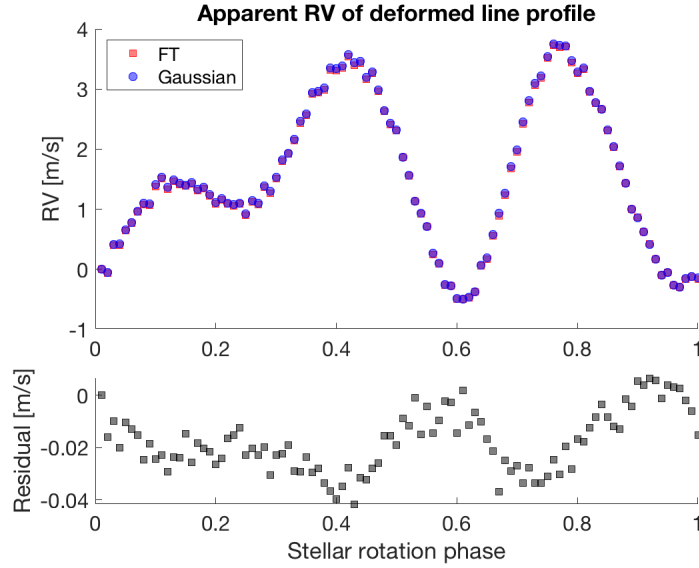


Fig. 2.8: Apparent RV of deformed line profile calculated with Fourier transform and Gaussian fit. Both results are also highly consistent with each other.

are plotted against rotation phase (Fig. 2.8). If we take the root-mean-squares of both RV_{FT} and RV_{Gaussian} to be the intrinsic noise level ($rms_{\text{FT}} = rms_{\text{Gaussian}} = 0.08$ m/s) corresponding $S/N = 10,000$, the uncertainty of $RV_{\text{FT}} - RV_{\text{Gaussian}}$ as residual would have an uncertainty of $\sqrt{rms_{\text{FT}}^2 + rms_{\text{Gaussian}}^2} \approx 0.11$ m/s, meaning that the residuals are 0 within uncertainty and showing that RV_{FT} and RV_{Gaussian} are indistinguishably consistent.

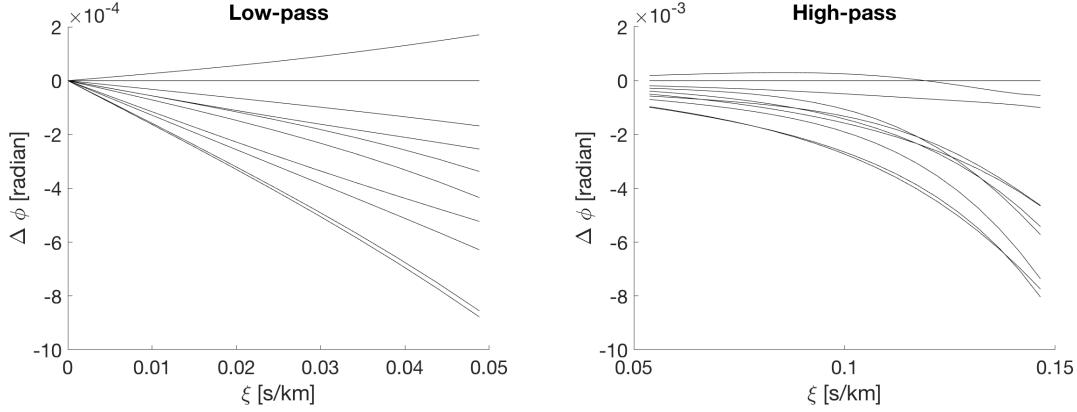


Fig. 2.9: Differential phase spectrum as shown in Fig. 2.7b sub-divided into lower frequency range and higher frequency range. Only the non-negative ranges are plotted.

Remark Using (almost) all the information in the power spectrum and the phase spectrum will end up with the same radial velocity as acquiring the line centroid fitted by a Gaussian line profile.

Although the intrinsic line deformation (in the absence of any velocity shift in the host star) does mimic the radial velocity shift, we note the shape and scale differences in the differential phase spectrum between an actual line shift (Fig. 2.3) and a line deformation (Fig. 2.7) – the latter becomes highly skewed as $|\Delta\phi|$ increases dramatically towards higher frequencies. Such differences provide key messages to differentiate the two circumstances.

For example, as Fig. 2.9 presents, if we divide (arbitrarily) the frequencies into low frequency range ($|\xi| < 0.06$ s/km; i.e. apply a low-pass filter) and high frequency range ($|\xi| > 0.06$ s/km; i.e. apply a high-pass filter)⁴, and compute the equivalent Fourier transformed radial velocity RV_{FT} for each, we would obtain two sets of radial velocities, one represents the radial velocity shifts (denoted as $RV_{FT,L}$) of the lower frequency components and the other (denoted as $RV_{FT,H}$) represents the higher.

We find, to our surprise, that both $RV_{FT,L}$ and $RV_{FT,H}$ are linearly correlated with the jitter (equivalent to RV_{Gaussian} in this case as no planets are present; Fig. 2.10), yet neither has a 1:1 correlation – $RV_{FT,H}$ demonstrates a higher response to jitter, with a slope $k_H = 1.8599$ in the linear fit, meaning the radial velocity shift of 1 m/s due to line deformation is detected as 1.8599 m/s shift on average using *this* high-pass filter;

⁴In this example, we limit the higher frequency range effective in $0.06 \text{ s/km} < |\xi| < 0.15 \text{ s/km}$, because frequencies higher than 0.15 s/km hardly contributes to the shape of the line profile (the power ~ 0), and they are also heavily impacted by noise.

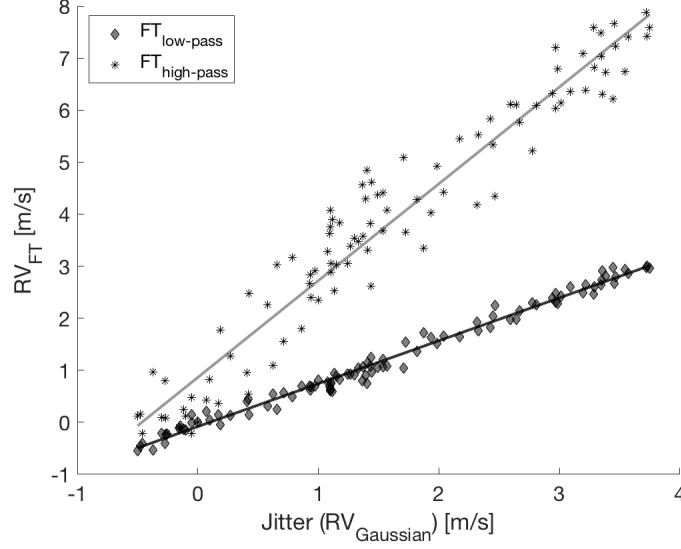


Fig. 2.10: Applying the low-pass and high-pass filters, the Fourier transform $RV_{\text{FT,L}}$ and $RV_{\text{FT,H}}$ are linearly correlated with the jitter (RV_{Gaussian}).

whereas $k_L = 0.8245$ for $RV_{\text{FT,L}}$, meaning such a 1 m/s deformation is detected as 0.8245 m/s shift on average using *this* low-pass filter. When we combine both filters, we would have obtained the 1:1 correlation as discussed above (Fig. 2.8).

We could further investigate how well this linearity behaves for each filter by scaling the measured $RV_{\text{FT,L}}$ and $RV_{\text{FT,H}}$ by their corresponding factors $1/k_L$ and $1/k_H$ respectively, and compare them with the jitter (RV_{Gaussian}), as presented in Fig. 2.11. The root-mean-squares of the residuals ($RV_{\text{FT,L/H}} - RV_{\text{Gaussian}}$) are $rms_{\text{FT,L}} \approx 0.15$ m/s and $rms_{\text{FT,H}} \approx 0.32$ m/s respectively. Not surprisingly, $rms_{\text{FT,H}} > rms_{\text{FT,L}}$, because in *this* case more information is concentrated in the low-pass filter (i.e. $\int_0^{0.05} |P| d\xi > \int_{0.05}^{0.15} |P| d\xi$ where P is the amplitude of the power spectrum). For this reason, $rms_{\text{FT,L}} - RV_{\text{Gaussian}}$ would be more stable and less scattered. If the bound between the low- and high-pass filter ξ_0 is chosen such that $\int_0^{\xi_0} |P| d\xi = \int_{\xi_0}^{0.15} |P| d\xi$, we would expect $rms_{\text{FT,H}} = rms_{\text{FT,L}}$.

Remark The apparent radial velocity shift due to spectral line deformation (i.e. jitter) can be seen as a mingle of one radial velocity shift in higher frequency components and one in lower frequency components. They are both, in the SOAP simulations, scaled with the jitter.

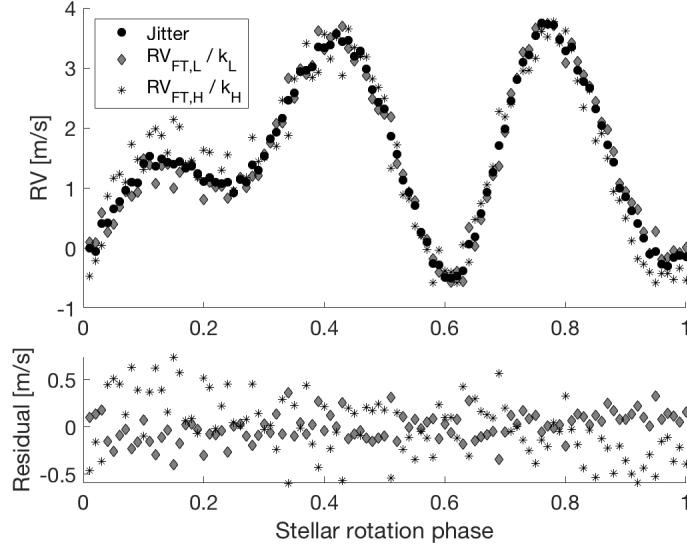


Fig. 2.11: Scaling the low-pass and high-pass Fourier transformed radial velocities to match the input jitter.

2.2.3 Jitter model

We have found in § 2.1 that RV_{FT} and RV_{Gaussian} demonstrate basically the same response to line shifts. For its linearity in the differential phase spectrum as a result of a line shift (Fig.2.3b), we can interpolate the conclusion to part of the differential phase spectrum, that is, both $RV_{\text{FT,H}}$ and $RV_{\text{FT,L}}$ will also have the same response as RV_{Gaussian} to a line shift. We have also found earlier in this section (§ 2.2) that $RV_{\text{FT,L}}$ CGT: *What range compared to, say, the line width of the line profile?* is less sensitive ($k_L = 0.8245$) to line deformation than RV_{Gaussian} , whereas $RV_{\text{FT,H}}$ is more sensitive ($k_H = 1.8599$).

We can therefore write the following measurable quantities – $RV_{\text{FT,L/H}}$ and RV_{Gaussian} – as the sum of corresponding contributions from a bulk shift in the star (which we hereafter assume to be due to a planet or planets), and variability in the stellar line profile (hereafter lumped under the general name “jitter”):

$$RV_{\text{Gaussian}} = RV_{\text{planet}} + RV_{\text{jitter}}$$

$$RV_{\text{FT,L}} = RV_{\text{planet}} + k_L \cdot RV_{\text{jitter}} \quad (2.10)$$

$$RV_{\text{FT,H}} = RV_{\text{planet}} + k_H \cdot RV_{\text{jitter}}. \quad (2.11)$$

Subtracting one from the other to remove RV_{planet} gives

$$RV_{\text{Gaussian}} - RV_{\text{FT,L}} = (1 - k_L) \cdot RV_{\text{jitter}} \quad (2.12)$$

$$RV_{\text{Gaussian}} - RV_{\text{FT,H}} = (1 - k_H) \cdot RV_{\text{jitter}} \quad (2.13)$$

$$RV_{\text{FT,H}} - RV_{\text{FT,L}} = (k_H - k_L) \cdot RV_{\text{jitter}}. \quad (2.14)$$

Note that only (any) two of them are independent equations, as the any one can be derived from the other two. Rearranging also yields two out of three independent expressions for the jitter model

$$RV_{\text{jitter}} = \frac{RV_{\text{Gaussian}} - RV_{\text{FT,L}}}{1 - k_L} \quad (2.15)$$

$$RV_{\text{jitter}} = \frac{RV_{\text{Gaussian}} - RV_{\text{FT,H}}}{1 - k_H} \quad (2.16)$$

$$RV_{\text{jitter}} = \frac{RV_{\text{FT,H}} - RV_{\text{FT,L}}}{k_H - k_L} \quad (2.17)$$

where RV_{Gaussian} , $RV_{\text{FT,L}}$ and $RV_{\text{FT,H}}$ are direct measurements, whereas k_L and k_H are unknowns but can be incorporated into the radial velocity models (Eq. 2.10 and Eq. 2.11) in the process of recovering planets. When there's no planet or the planetary radial velocity signal is negligible compared with the size of jitter, $RV_{\text{FT,L}}$ and $RV_{\text{FT,H}}$ will be proportional to RV_{jitter} (Example: §2.3.1).

2.2.4 Testing the recovery of Jitter

We again performed tests to see if we can correctly recover artificially generated model jitter using our new technique (Eq. 2.15 to Eq. 2.17).

We generated 200 deformed line profiles (in the form of cross-correlation functions) using SOAP 2.0. All the configurations are the same as used in §2.2.2, except that they are evenly sampled throughout two rotation periods. The jitter amplitude is roughly 2 m/s. In addition, each line profile is further shifted by an amount RV_{planet} appropriate for a planet generating a Keplerian orbit in the star of the amplitude

$$A_{\text{planet}} = 2 \text{ m/s}$$

and a planetary orbital period to stellar rotation period ratio of 0.7;

$$\frac{\nu_{\text{orb}}}{\nu_{\text{rot}}} = \frac{P_{\text{rot}}}{P_{\text{orb}}} = 0.7.$$

In principle, the RV_{planet} configuration shouldn't matter much because it will be mostly cancelled out *CGT: cancelled? Or swamped?* in the jitter model.

We then obtain two sets of radial velocities for each simulated profile: RV_{Gaussian} and RV_{FT} , which are reproduced in the upper panel of Fig. 2.12. As we know the amount of input jitter in our simulation, we simply scale up ΔRV by a parameter α to match the input jitter (dashed line in middle panel). *CGT: You've lost me here ...* The jitter model (black dots in middle panel) becomes more scattered as $\alpha \gg 1$. As a result, a moving average modulated by a Gaussian kernel is implemented to smooth out the data (solid line in middle panel).

CGT: I'm confused - whats the difference between input jitter and model jitter?

To examine the performance, we compare the rms of the input jitter rms_{jitter} and the rms of the residual between the input jitter and the model jitter rms_{residual} . The former can be treated as the scatter after fitting the correct planet(s) without jitter correction, while the latter can be treated as the scatter after the additional jitter is removed. The rms *CGT: of what? which one?* is reduced from $rms_{\text{jitter}} = 1.22$ m/s to $rms_{\text{residual}} = 0.70$ m/s, which is crucial in enhancing the detection of planets with radial velocities of sub-m/s amplitudes. However, we should also note that there are systematic differences between the input jitter and our model jitter (i.e. the residual sorts of repeats itself in the two stellar rotation periods).

We should be aware that while removing the stellar variability contribution from the data, it may also add in some remnant features. *CGT: I'm afraid this is a sort of meaningless statement.*

2.2.5 End-to-end Simulations

Unless we are sure of a null-planetary system where $RV_{\text{planet}} = 0$ and from Eq. ?? and Eq. ?? we obtain

$$k = RV_{\text{jitter}}/RV_{\text{Gaussian}}, \quad (2.18)$$

normally k cannot be directly calculated, so neither can α be. However, we could substitute the jitter model (Eq. ??) into Eq. ??, such that

$$RV_{\text{Gaussian}} = RV_{\text{planet}} + \alpha \cdot \Delta RV \quad (2.19)$$

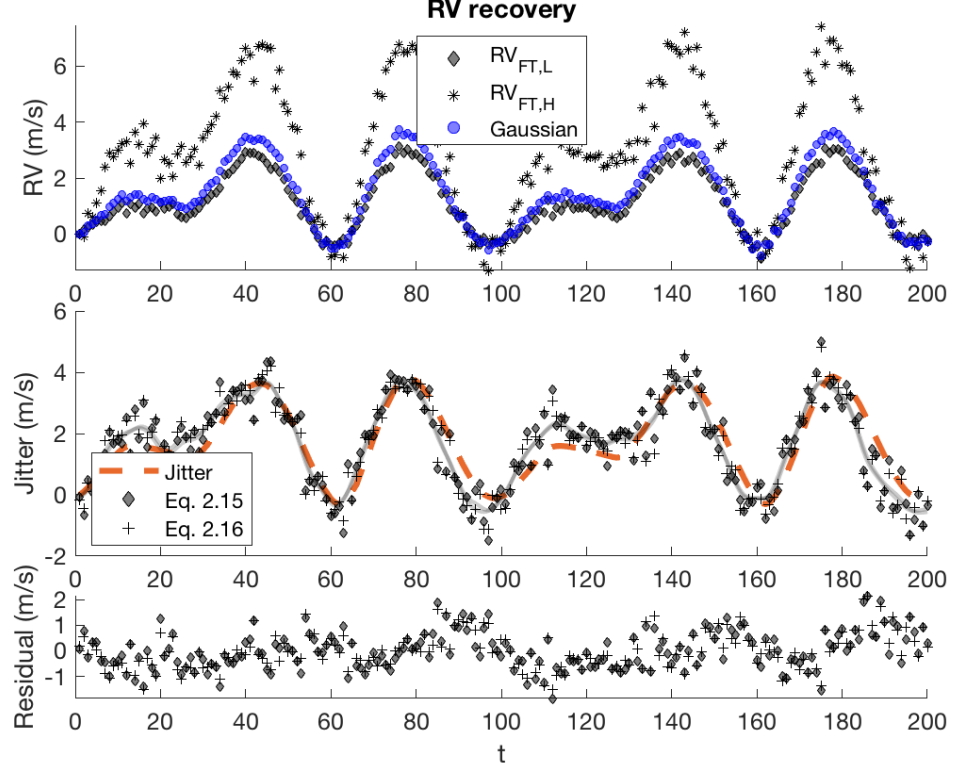


Fig. 2.12: Construct jitter model from simulation data.

where RV_{planet} is parametrised by Keplerian orbit(s) and both RV_{Gaussian} and ΔRV are measurable.

The tests are divided into two groups for comparison:

1. Fit RV_{Gaussian} by Keplerian orbit alone;
2. Fit RV_{Gaussian} by Keplerian orbit + jitter model (i.e. $\alpha \cdot \Delta RV$).

The injected planet has the same parameter settings as in §2.2.4, i.e. circular orbit with amplitude $A = 2$ m/s, orbital frequency ratio $\nu = 0.7$ and initial phase $\omega = 1$ rad. We will compare which group recovers the planet parameters better.

To better simulate the real observations, 40 data samples out of 200 from the two rotation periods are randomly selected. The fitting is achieved by running MCMC to maximise the log-likelihood function given the model. For the simulation, each radial velocity data is equally weighted (as they have the same S/N). It is defined if the input

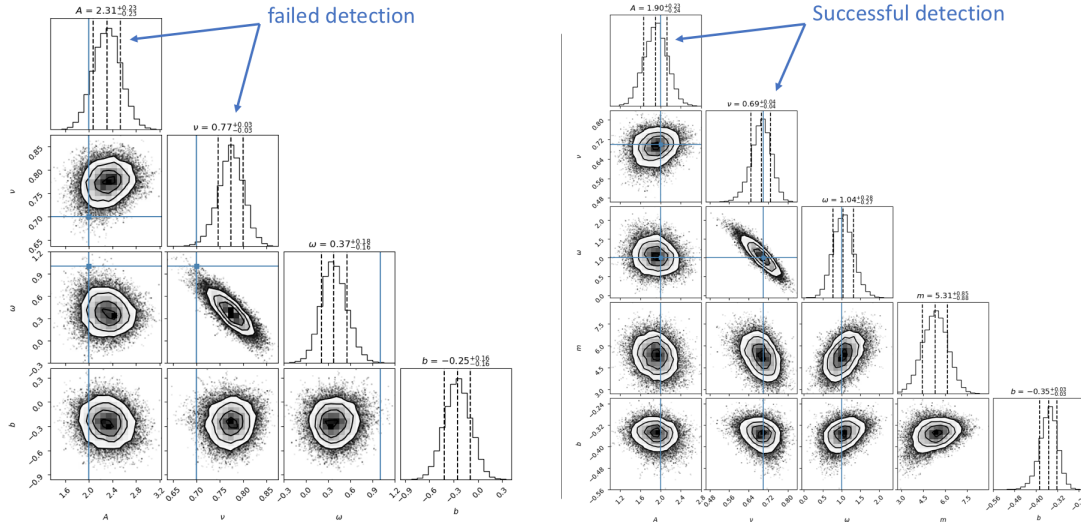


Fig. 2.13: Corner plots of MCMC. These are two examples of the output of MCMC: no jitter correction on the left and with jitter correction on the right. The input parameters are highlighted in the blue solid line. The three dashed lines of each histogram indicate the median and 1σ on both sides. On the left panel both blue lines of A and ν are outside the 1σ region, therefore it counts as a “failed detection”; on the right panel, it counts as a successful detection within 1σ .

parameter lies within 1σ errorbar of the output parameter, it counts as a successful detection.

For demonstration, we show one of the outputs in corner plots (Fig. 2.13) and the corresponding radial velocity fitting (Fig. 2.14). The corner plot visually shows the how the walkers explore the parameter space and their distribution. The histogram gives an example explaining how a “successful detection” is qualified. The radial velocity fitting plot demonstrates an example that implementing the jitter model effectively accounts for the spurious signals in the raw radial velocity data, reducing the rms from 1.14 m/s to 0.55 m/s.

In the end, we run 100 trails for the end-to-end simulation. The random differences among these 100 trails come from:

- photon noise given the S/N;
- randomly selected 40 samplings in the 200 line profiles.

It turns out that in 46% of the 100 trails are successful detections for both A and ν when we apply the jitter correction model, while this percentage is only 11% without jitter

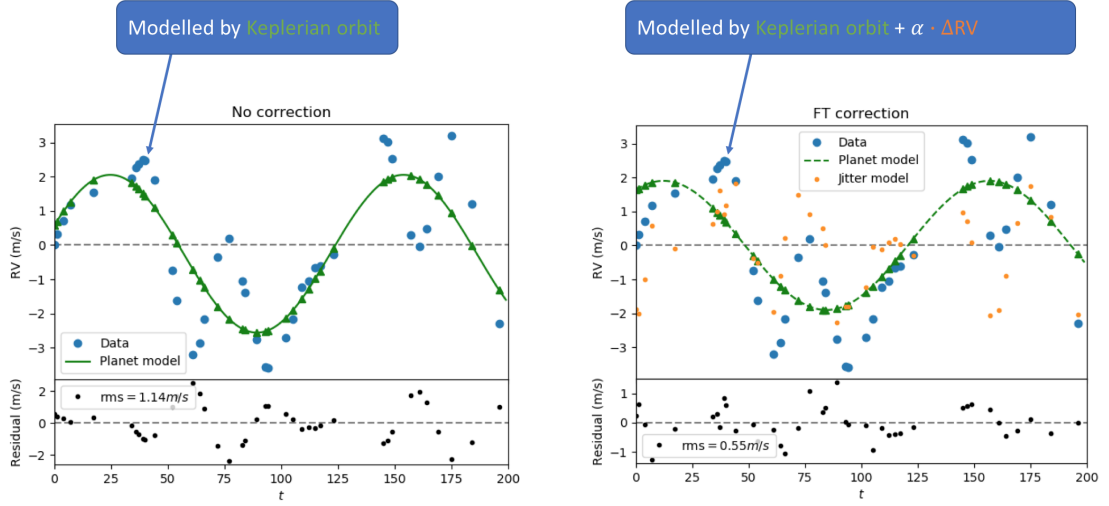


Fig. 2.14: Radial velocity fitting. These are two fittings that comes out from the MCMC corner plots in Fig. 2.13. On the left panel without jitter correction, we can see that the input jitter increases the scatter of the raw radial velocities, resulting in an overestimated amplitude A ; while on the right panel with jitter correction, the additional input jitter is accounted for by the jitter model.

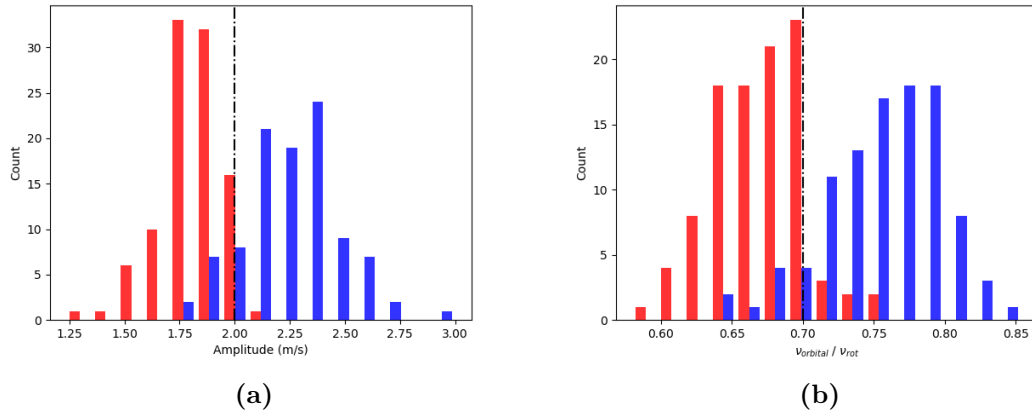


Fig. 2.15: Distribution of recovered parameters. The red are results of jitter correction by Fourier transform; The blue are results of no jitter correction.

correction. In more detail, Fig. 2.15 shows that with jitter correction (in red), both of the amplitude and orbital frequency ratio tend to be underestimated, which is shown opposite for the results without correction (in blue). Moreover, the jitter corrected parameters are better constrained (i.e. with narrower distributions) and performs much better in ν than without correction. While it is tempting to say the correct answer is more likely in between the results from these two fittings, we would need more tests to conclude.

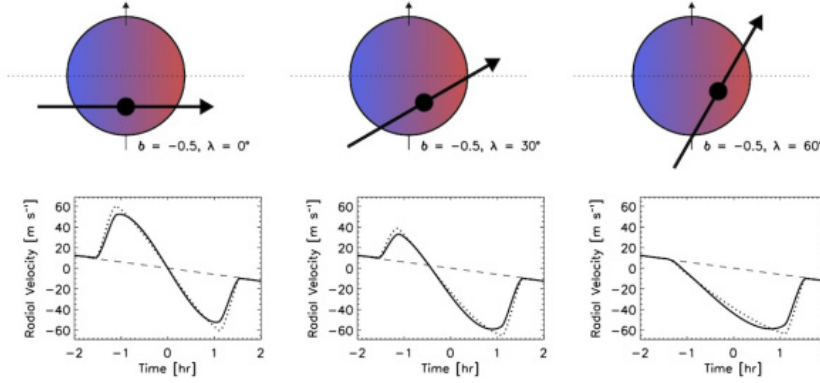


Fig. 2.16: Demo: Rossiter–McLaughlin effect (reference...). It is a apparent radial velocity change of the parent star due to an eclipsing binary (whether star or planet) that breaks the observed flux symmetry in the stellar photosphere, resulting in imbalanced redshift and blueshift. It shows in this plot three different star-planet alignments that causes three corresponding different shapes of radial velocity curve, and hence the radial velocity curve sheds information on the geometry of the alignment.

2.3 Fourier transform with real observations

2.3.1 HD189733: Rossiter–McLaughlin effect as jitter

HD189733 is a well studied binary star system. The main star HD189733 A is known to host a gas giant exoplanet HD189733 b, first detected by transits (reference...) and later by Doppler spectroscopy (references...). It was also the first exoplanet transit observed in X-ray (references...).

We choose this target for the following reasons:

- The exoplanet is well confirmed;
- The host star is bright enough: $m_V = 7.66$;
- The gas giant exoplanet causes a prominent apparent radial velocity while it transits (~ 40 m/s) due to Rossiter–McLaughlin effect.

We treat as if it were an “active” star with one big dark starspot, as the Rossiter–McLaughlin effect causes the line profile deformed in a similar manner that a starspot would do (Fig. 2.16). We aim to test if our jitter model can account for the radial velocity variation from Rossiter–McLaughlin effect.

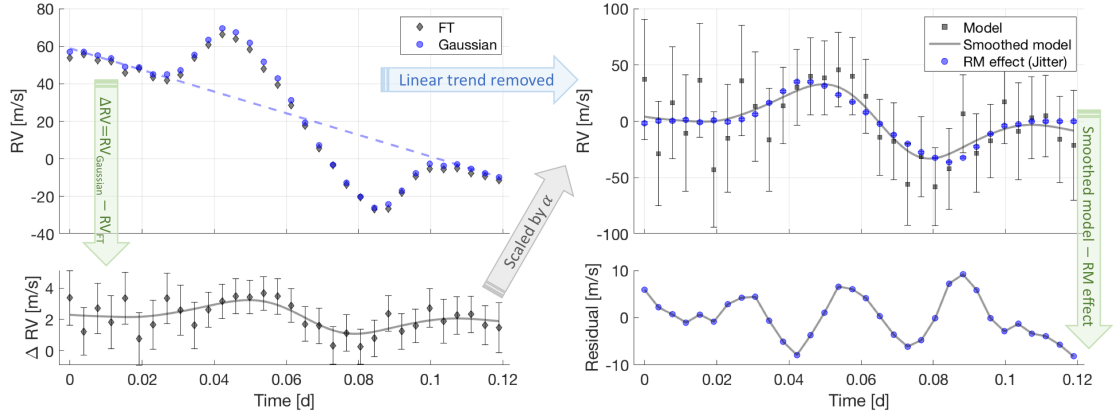


Fig. 2.17: HD189733: removal of Rossiter–McLaughlin effect as jitter. From RV_{Gaussian} and RV_{FT} to ΔRV . The scattered ΔRV are smoothed by applying a moving average with a Gaussian filter and further weighted according to the size of errorbar. It is then scaled by α to match the jitter (in this case the radial velocities of the observed Rossiter–McLaughlin effect). The residual is the difference between the smoothed jitter model and the observed Rossiter–McLaughlin effect. Errorbars are not plotted for the residuals for the reason that they will overwhelm the residual themselves.

The procedure is rather standardized. Both RV_{Gaussian} and RV_{FT} are calculated from the HARPS cross-correlation functions of the spectra. $\Delta RV = RV_{\text{Gaussian}} - RV_{\text{FT}}$ are then smoothed by a Gaussian filter. The prototype of the Rossiter–McLaughlin radial velocity curve is already identifiable (ΔRV of the lower panel of Fig. 2.17).

During transit, as the parent star and the exoplanet are along the line of sight, there will be no contribution to radial velocity by the orbiting exoplanet. However, the radial velocity shows an inclined trend in this system. It is due to the other orbiting star in the binary star system. Considering the orbital period of the binary star estimated around 3,200 years (reference...), the radial velocity contribution from the other star during the timespan of transit (~ 0.08 days) can be treated linear. By removing such a linear trend, which is fitted for the non-transiting part, we can extract the observed Rossiter–McLaughlin radial velocity curve. It is treated as jitter and modelled by $\alpha \cdot \Delta RV$ (Fig. 2.17 upper right). Note that the errorbars of the jitter model also becomes a factor of α ($\alpha \gg 1$) larger; however, the model itself shows a descent approximation of the Rossiter–McLaughlin radial velocity curve. The difference between our modelled jitter and the observed Rossiter–McLaughlin effect peaks at ~ 10 m/s, a $\sim 75\%$ removal of the jitter from ~ 40 m/s.

Remarks The effective length of the smoothing kernel should be carefully chosen. In this case, it's chosen most effective within roughly one neighbouring data point on both size. While mitigating the effect of noise (especially for relatively lower S/N data outside the transits), to which the Fourier transform is sensitive, it also smears the drastic velocity change when the planet ingresses and egresses the stellar disk. To solve this awkward situation, an adaptive (i.e. S/N dependent) effective length of the smoothing kernel may be used.

2.3.2 Examples 2

HD 49933 is an F2 main sequence star with an apparent magnitude of $m_V = 5.8$ ([1]),

2.3.3 Example 3

A float barrier will stop figures from going beyond this point. They are handy to make sure they don't go into the next section.

2.4 References

- [1] S. Malaroda. Study of the F-type stars. I. MK spectral types. *aj*, 80:637–641, August 1975. 24